How to cite: *Angew. Chem. Int. Ed.* **2022,** *61,* e202211216
International Edition: doi.org/10.1002/anie.202211216
German Edition: doi.org/10.1002/ange.202211216

Metal–Organic Frameworks

Facet Engineering of a Metal–Organic Framework Support Modulates the Microenvironment of Palladium Nanoparticles for Selective Hydrogenation

*Ming-Liang Gao, Luyan Li, Zi-Xuan Sun, Jia-Rui Li, and Hai-Long Jiang**

Abstract: The exposed facets of supported catalysts play a crucial role in catalysis; however, they are usually ignored and related studies remain rare. Herein, we have fabricated a series of sandwich-structured metal–organic framework composites, denoted ZIF-8_X@Pd@ZIF-8 (x represents the morphology of ZIF-8 core, i.e., ZIF-8_C exposing (100) facet, ZIF-8_{RD} exposing (110) facet, and ZIF-8_{TRD} exposing mixed (100) and (110) facets), featuring Pd nanoparticles deposited on the specific crystal facets of ZIF-8 core, for hydrogenation of *p*-chloronitrobenzene. The Pd electronic state is tailored by the ZIF-8 core, where more electron-deficient Pd is found in ZIF-8_C@Pd@ZIF-8 than that in ZIF-8_{RD}@Pd@ZIF-8, leading to discriminative adsorption of the $-NO_2$ and –Cl groups of *p*-chloronitrobenzene. Consequently, ZIF-8_C@Pd@ZIF-8 exhibits excellent activity (97.6%) and selectivity (98.1%) to *p*-chloroaniline. This work highlights crystal facet engineering of supports to modulate the microenvironment and electronic state of supported metal nanoparticles, offering a promising avenue to enhanced catalysis.

Introduction

Selective hydrogenation of halonitrobenzene to the corresponding haloaniline is widely employed to produce vital organic intermediates for various polymers, pharmaceuticals, fine chemicals, etc.[1] Improving the catalytic activity, and particularly the selectivity, of halonitrobenzene to haloaniline conversion remains a great challenge. A variety of supported noble-metal catalysts,[1,2] such as Pd,[1a,2a] Pt,[1c,2b,c] and Au,[2e,f] have been investigated for selective hydrogenation of halonitrobenzene. However, dehalogenation always occurs in the hydrogenation reaction process. To achieve high activity and selectivity in halonitrobenzene hydrogenation, the dehalogenation reaction should be suppressed as much as possible. Therefore, the development of high-performance supported metal catalysts for selective hydrogenation of halonitrobenzene is highly desired.

Supported metal catalysts are intensively adopted in a wide range of heterogeneous catalytic reactions.[3] In recent decades, much research effort has been devoted to the investigation of the influence on catalytic performance by tailoring the metal nanoparticles (NPs), such as size, alloying, morphology, etc., or controlling the support microstructures.[4] By contrast, the crystal facet control of the support, an important influencing factor for catalysis, has long been neglected.[3c] The crystal facets exposed on the supports are able to affect the physicochemical properties of the supported metal catalyst because of variations in the local (interfacial) microenvironment around metal sites, thereby improving the catalytic performance.[5] To date, improved catalysis by facet engineering of the supports is usually influenced by multiple mutual factors,[6] including 1) the size effect of the supported metal NPs,[6a,b] 2) support-engaged substrate activation,[6c] 3) structural sensitivity of strong metal-support interactions,[6d] and so on. As these factors are tangled together in the supported catalysts, it is difficult to reach a precise understanding of how the catalytic performance of metal NPs is affected by the support crystal facet as the only perturbation. To gain exact and deep insights into the facet effect of supports, it is necessary to construct model systems of metal nanoparticulate catalysts on desired supports that are able to expose diverse crystal facets with definite compositions and structures, excluding the interference factors. Meanwhile, given that the interaction between metal NPs and diverse crystal facets is usually different, this possibly leads to peeling off of metal NPs from the supports when the interaction is weak. To address this issue, the sandwich-structured catalysts, of which the original supported catalysts are covered by a coating layer with the same support composition, would be favorable to the stabilization of metal NPs.[7] This raises a new demand for porous supports to guarantee accessibility to the sandwiched metal NPs.

To meet the above requirements for the supports, metal–organic frameworks (MOFs), an emerging class of crystalline porous materials with high porosity and tunability, are promising candidates.[8] The structure, size, and morphology of MOFs can be well controlled to manifest well-defined crystal facets. In particular, it is feasible to control all other structural parameters with crystal facets as the only variable in the MOF supports, which provides an ideal model to explore the structure-performance relation-

[*] Dr. M.-L. Gao, Dr. L. Li, Z.-X. Sun, J.-R. Li, Prof. Dr. H.-L. Jiang
Department of Chemistry, University of Science and Technology of China, Hefei
Anhui 230026 (P.R. China)
E-mail: jianglab@ustc.edu.cn
Homepage: http://staff.ustc.edu.cn/~jianglab/

ship of the supported metal catalysts. Moreover, although MOFs adopted to support metal NPs are intensively reported for catalysis,[3d,9] to our knowledge, the facet effect of MOF supports has not yet been investigated.

In this work, a representative MOF is adopted—zeolite imidazolate framework-8 (ZIF-8)[10]—featuring a sodalite structure that can be regulated to expose different facets, including the (100) facet of ZIF-8_C, (110) facet of ZIF-8_{RD}, and mixed (100) and (110) facets of ZIF-8_{TRD1} and ZIF-8_{TRD2}. The ZIF-8 with different morphologies were adopted to support Pd NPs, followed by coating a thin protective layer of ZIF-8 shell, affording the sandwich-structured ZIF-8_X@Pd@ZIF-8 composites (X indicates the specific morphology of the ZIF-8 core) (Scheme 1). Different crystal facets of ZIF-8 afford particular chemical microenvironments (Zn^{2+} node on the (100) facet and the linker on the (110) facet) for Pd NPs.[11] The (100) crystal facet results in more electron-deficient Pd than that of the (110) facet, which can be attributed to the interaction between the Pd and exposed Zn^{2+} ions on the (100) facet of ZIF-8. Consequently, ZIF-8_C@Pd@ZIF-8 with electron-deficient Pd species exhibits excellent activity and selectivity in the hydrogenation of halonitrobenzenes to haloanilines. To our knowledge, this is the first work that regulates the electronic properties of metal NPs supported by MOF facet engineering for enhanced catalytic performance.

Results and Discussion

The representative MOF, ZIF-8 (also called MAF-4),[10] was chosen due to its high stability and tunable crystal facets. Rhombic dodecahedral (RD) ZIF-8 (denoted ZIF-8_{RD}), with linkers on the exposed (110) facets, was prepared by mixing $Zn(NO_3)_2$ and 2-methylimidazole (2-MIM) in deionized water without additive.[11b] The cubic ZIF-8 (denoted ZIF-8_C), with Zn^{2+} nodes on the exposed (100) facets,[11c] was synthesized by adding cetyltrimethylammonium bromide (CTAB) as a structure-directing agent. (Figure S1).

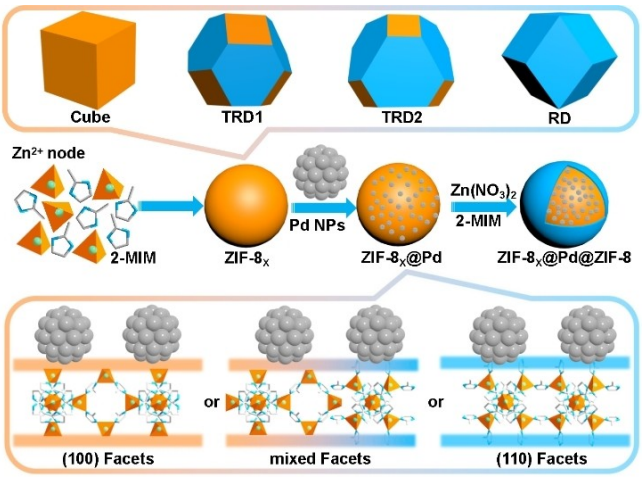

Scheme 1. Illustration of the synthetic strategies for the sandwich-structured ZIF-8_X@Pd@ZIF-8 composites.

Moreover, the truncated rhombic dodecahedral ZIF-8 (denoted ZIF-8_{TRD}) with different ratios of exposed (100) and (110) facets, in which the ratios of approximately 0.69 and 0.38 are related to ZIF-8_{TRD1} and ZIF-8_{TRD2}, respectively, can also be obtained by regulating the amount of CTAB (Figure S1).[11b] In the above processes of MOF crystal growth, CTAB selectively attaches to the (100) facets of ZIF-8 and causes their exposure. The crystal structures and exposed facets of the above ZIF-8_X crystals are evaluated by powder X-ray diffraction (XRD) patterns and the results suggest that all obtained ZIF-8_X with different facets possess good crystallinity (Figure 1a, Figure S2a). From ZIF-8_{RD} to ZIF-8_C, the gradually increased intensity of the (200) diffraction peak indicates the incremental exposure ratio of the (100) facet, while the (110) peak with reduced intensity support the decreased exposure of (110) facets (Figure 1a, Figure S2a). Moreover, ZIF-8 possesses a positively charged surface in pure water; ZIF-8_C possesses the maximum zeta potential (31.8 mV), more than ZIF-8_{TRD1} (27.3 mV), ZIF-8_{TRD2} (19.7 mV) and ZIF-8_{RD} (14.7 mV), and in line with the fact that Zn^{2+} nodes are exposed on the surface of ZIF-8_C whereas the linkers are exposed on ZIF-8_{RD} (Figure S3).

The Pd NPs with sizes of 3.7 ± 0.6 nm were pre-synthesized by a PVP-assisted process (Figure S4).[12] By employing the above ZIF-8_X with different exposed facets as

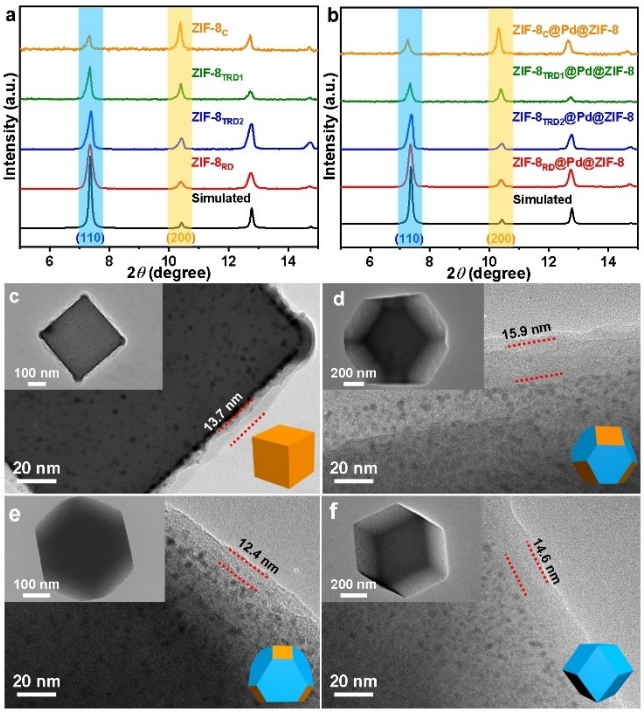

Figure 1. Powder XRD patterns of the four kinds of a) ZIF-8_X core and b) ZIF-8_X@Pd@ZIF-8 composites. TEM images of c) ZIF-8_C@Pd@ZIF-8, d) ZIF-8_{TRD1}@Pd@ZIF-8, e) ZIF-8_{TRD2}@Pd@ZIF-8, f) ZIF-8_{RD}@Pd@ZIF-8. Insets in (c)–(f): top left, the morphology of an enlarged single particle of ZIF-8_X@Pd@ZIF-8; bottom right, illustration of ideal morphology with exposed specific facets for ZIF-8_X@Pd@ZIF-8.

the supports to deposit the pre-synthesized Pd NPs, followed by further epitaxial growth of a thin ZIF-8 shell to yield sandwich-structured ZIF-8_X@Pd@ZIF-8 composites. Powder XRD patterns of ZIF-8_X@Pd@ZIF-8 demonstrate that the ZIF-8 crystallinity is well maintained, indicating that the introduction of Pd NPs does not change its integrity. The intensity trends of (110) and (200) peaks are similar to those of ZIF-8_X (Figure 1b, Figure S2b). Inductively coupled plasma atomic emission spectrometry (ICP-AES) results indicate that the loading amount of Pd NPs in these composites were ~2.6 wt% (Table S1). Scanning electron microscopy (SEM) images of ZIF-8_X@Pd@ZIF-8 indicate that the size and morphology of the original ZIF-8_C, ZIF-8_{TRD1}, ZIF-8_{TRD2}, and ZIF-8_{RD} composites are almost inherited in the resulting composites, except for the wrinkled thin layers on the samples due to the thin coatings of ZIF-8 shell (Figure S5). Transmission electron microscopy (TEM) observations support the sandwich nanostructure of these composites, in which the small-sized Pd NPs are well encapsulated in the ZIF-8 coating layer with similar thicknesses of 12–16 nm (Figure 1c–f, Figure S6). Nitrogen sorption experiments reveal that all ZIF-8_X and ZIF-8_X@Pd@ZIF-8 composites display high porosity and similar Brunauer–Emmett–Teller (BET) surface areas (approximately 1310–1060 $m^2 g^{-1}$) and pore size distributions (Figures S7–S10). The slight decrease in surface area compared to the ZIF-8 core is ascribed to the Pd mass occupation.

Thanks to the successful preparation of the above composites, the surface interaction between ZIF-8_X and Pd NPs in ZIF-8_X@Pd@ZIF-8 composites was first investigated by X-ray photoelectron spectroscopy (XPS) (Figure 2a). The Pd $3d_{5/2}$ peak in ZIF-8_C@Pd@ZIF-8 shifts to higher binding energy at 335.04 eV compared to that in ZIF-8_{RD}@Pd@ZIF-8 (334.81 eV). Overall, the electron deficiency of Pd follows the order ZIF-8_C@Pd@ZIF-8 > ZIF-8_{TRD1}@Pd@ZIF-8 > ZIF-8_{TRD2}@Pd@ZIF-8 > ZIF-8_{RD}@Pd@ZIF-8. To further validate the discriminative Pd electronic states in ZIF-8_X@Pd@ZIF-8, the diffuse reflectance infrared-Fourier transform (DRIFT) spectra of CO adsorption were collected. The spectra reveal the coexistence of two modes of CO adsorption, in which the pronounced band at 2020–2055 cm^{-1} is assignable to the C–O vibration of linearly adsorbed CO, and the band at 1850–1950 cm^{-1} corresponds to the bridge-bonded peak of the CO molecule.[13] The shift of the linearly adsorbed CO peak in the four composites (i.e., the peak gradually increasing from 2020.8 cm^{-1} for ZIF-8_{RD}@Pd@ZIF-8 to 2054.3 cm^{-1} for ZIF-8_C@Pd@ZIF-8) supports the differentiated electronic states of interfacial Pd with varying ZIF-8 facets (Figure 2b).[14] The electrons of Pd species are injected into the 2π* orbitals of CO (electron backdonation), and different electronic states of Pd NPs give rise to different Pd-CO adsorption and the corresponding DRIFTS wavenumber. Based on the CO-DRIFTS results, electron-deficient Pd species in ZIF-8_C@Pd@ZIF-8 inject fewer electrons into the 2π* orbitals of CO, resulting in a peak shift to a higher wavenumber. By contrast, the electron-rich Pd species in ZIF-8_{RD}@Pd@ZIF-8 inject more electrons into the 2π* orbitals of CO, leading to a peak shift to a lower wavenumber. The results on the electron deficiency trend are in good agreement with the above XPS results. The reason behind this trend of Pd electron deficiency is ascribed to the modulated microenvironment around Pd created by the altered exposed facets of ZIF-8 in these composites. The ZIF-8_C crystals are composed of six (100) facets with Zn^{2+} nodes exposed,[11a] while the ZIF-8_{RD} crystals are bounded by twelve (110) facets with the linker exposed.[11c] Therefore, the discriminative Pd electronic states are actually attributed to unequal interactions between Pd and different facets of ZIF-8, in which the interface between the Zn^{2+} node on the (100) facet and Pd results in stronger interfacial interactions and more electron transfer from the Pd to the MOF than that of the linker on the (110) facet (Figure 2c).

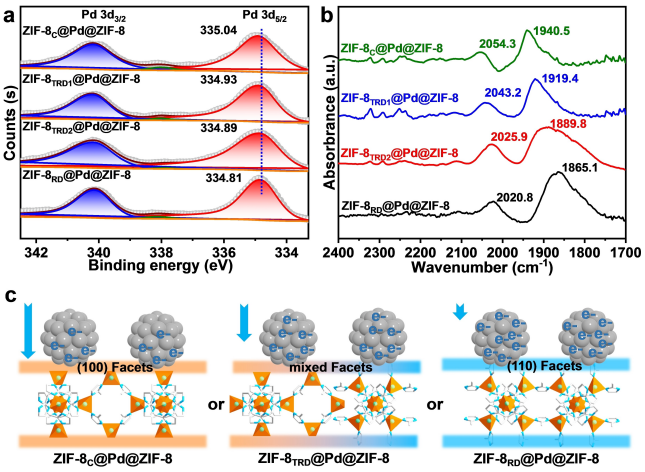

Figure 2. a) The Pd 3d XPS spectra for ZIF-8_X@Pd@ZIF-8. b) DRIFT spectra of CO adsorption on Pd NPs from ZIF-8_x@Pd@ZIF-8 in a flowing 10% CO/Ar mixed gas atmosphere. c) Diagram showing the discriminative interfacial electron transfer between (100) or (110), or mixed facets of ZIF-8 and Pd NPs. The arrow length represents the level of electron transfer from Pd to the support.

To understand the influence of the MOF crystal facets on the catalysis of the supported Pd NPs, the hydrogenation of *p*-chloronitrobenzene (*p*-CNB) over ZIF-8_X@Pd@ZIF-8 in the presence of hydrazine hydrate as the hydrogen source was attempted (Table 1). The ZIF-8_C@Pd@ZIF-8 displays preeminent conversion (97.6%) of *p*-CNB and selectivity (98.1%) to *p*-CAN at 85 °C (Table 1, entry 1). Significantly, by adopting the other composites with identical sizes and locations of Pd NPs, yet different facets of the ZIF-8 core, lower activities and selectivities were observed for ZIF-8_{TRD1}@Pd@ZIF-8 (74.2%, 85.3%), ZIF-8_{TRD1}@Pd@ZIF-8 (58.7%, 76.2%), and ZIF-8_{RD}@Pd@ZIF-8 (47.0%, 62.4%) compared to ZIF-8_C@Pd@ZIF-8, thereby unambiguously demonstrating the significant role of the crystal facet of the ZIF-8 core in the reaction (Table 1, entries 2–4). The higher activity of ZIF-8_C@Pd@ZIF-8 can be attributed to its electron-deficient Pd species, which would enhance the adsorption of the electron-rich $-NO_2$ group of *p*-CNB and favor the attack of N=O bonds through a nucleophilic process.[9e,15] Moreover, the straightforward one-step adsorption of the $-NO_2$ group is responsible for the superior

Table 1: Selective hydrogenation of *p*-CNB over different catalysts.[a]

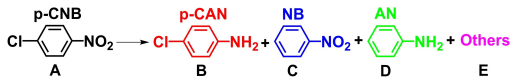

Entry	Catalyst	Conv. [%]	Sel. [%]			
			B	C	D	E
1	ZIF-8_C@Pd@ZIF-8	97.6	97.1	1.4	0.5	–
2	ZIF-8_{TRD1}@Pd@ZIF-8	74.2	85.3	11.2	0.5	–
3	ZIF-8_{TRD2}@Pd@ZIF-8	58.7	76.2	13.6	8.5	–
4	ZIF-8_{RD}@Pd@ZIF-8	47.0	62.4	25.3	12.3	–
5[b]	ZIF-8_C@Pd@ZIF-8	>99	98.9	–	1.1	–
6	ZIF-8_C	n.d.	–	–	–	–
7	No catalyst	n.d.	–	–	–	–
8	Pd/C	98	–	–	99	–
9	Pd/Al_2O_3	97.3	36.7	14.5	6.8	42.0
10	Pd/ZnO	83.9	75.9	5.3	3.3	15.5

[a] Reaction conditions: catalyst (10 mg), *p*-CNB (0.1 mmol), $T = 85\,^{\circ}C$, hydrazine hydrate (50 μL), MeCN (5 mL), Time = 60 min. [b] Extending reaction time to 3 h.

activity of ZIF-8_C@Pd@ZIF-8; by contrast, two-step adsorption and activation of both $-NO_2$ and C–Cl groups occur for the other composites, where the necessary molecular rotation of *p*-CNB around Pd sites in limited space takes time,[16] reasonably resulting in their reduced activity. By prolonging the reaction time to 3 h, the selectivity to *p*-CAN over ZIF-8_C@Pd@ZIF-8 can be maintained (Table 1, entry 5), proving the superiority of the catalyst. Moreover, the transport limitation imposed by the ZIF-8 shell in ZIF-8_C@Pd@ZIF-8 can be excluded by examining the conversion dependence on the catalyst amount (Figure S11). Notably, when a mixture of nitrobenzene and chlorobenzene is used, only aniline (AN) is observed as the product; no reaction occurs when the pure chlorobenzene is introduced (Table S2, entries 1–3). These results indicate that ZIF-8_C@Pd@ZIF-8 is active in the hydrogenation of nitrobenzene yet is inert for dechlorination under the present conditions. This further supports the catalyst favoring the reduction of the $-NO_2$ group rather than the activation of the C–Cl group. Given that the reaction does not proceed in the presence of ZIF-8 or the absence of catalyst, Pd NPs are proven to be the active sites for this reaction (Table 1, entries 6 and 7). When other supported Pd catalysts, including the commercial Pd/C and the common Pd/metal oxides, are introduced into the system, unfortunately, the dechlorination process occurs readily (Table 1, entries 8–10), generating AN as a side product and leading to unsatisfactory selectivity. These results demonstrate that ZIF-8_C@Pd@ZIF-8 possesses extraordinary advantages in this conversion with both high activity and high selectivity to *p*-CAN, which is assumed to be the contribution by the specific facet of ZIF-8_C for supported Pd NPs.

To elucidate the facet effect nature of the MOF support, Pd@ZIF-8_C encapsulating Pd NPs in ZIF-8 particles was deliberately prepared, exhibiting inferior catalytic conversion (62.3 %) and selectivity (67.2 %) to the targeted *p*-CAN compared to ZIF-8_C@Pd@ZIF-8, suggesting the importance of the interface microenvironment of exposed specific ZIF-8 facets around Pd NPs (Table S3, entry 1). The Pd NPs without any support offer sound conversion (71.6 %) and all selectivity to the dechlorination products (Table S3, entry 2). While ZIF-8_C@Pd with Pd NPs supported on ZIF-8_C exhibits a moderate conversion of 49.5 %, on account of the unavoidable Pd agglomeration in the absence of the ZIF-8 shell; the high selectivity (97.2 %) further highlights the significant role of the interfacial (100) facet around Pd NPs (Table S3, entry 3). In addition, all possible gaseous products (i.e., N_2, H_2 and NH_3) have been further analyzed by using ZIF-8_C@Pd@ZIF-8 as a catalyst (Figure S12).[17] When hydrazine is added to the reaction system in the absence of substrate, NH_3 is the main gaseous product and its concentration is identified by using the indophenol blue method (Figures S13, S14a).[18] By sharp contrast, the NH_3 product becomes negligible if both substrate and hydrazine are introduced (Figure S14b). The results imply that distinct reaction pathways occur in the above processes and the addition of substrate greatly promotes the reaction toward the N_2 generation pathway (Figure S15). Surprisingly, no H_2 product is detected accompanying N_2, suggesting that the active H* species instead of H_2 could be generated and stabilized on the Pd surface (Figure S15). Accordingly, the substrate reduction might occur through a direct transfer hydrogenation route from hydrazine to $-NO_2$ groups to afford *p*-CAN.[17b]

The superior activity and selectivity of ZIF-8_C@Pd@ZIF-8 encouraged us to investigate its stability and recyclability. Remarkably, ZIF-8_C@Pd@ZIF-8 shows stable catalytic performance in three consecutive recycling tests (Figure S16). No apparent loss of MOF crystallinity is observed in the powder XRD pattern after catalysis (Figure S17). Moreover, the morphology of ZIF-8_C@Pd@ZIF-8 is well retained after three cycles of catalysis (Figure S18). Importantly, the hot filtration experiment shows that no further conversion is observed after removing ZIF-8_C@Pd@ZIF-8 (Figure S19), indicating the true heterogeneous process and the absence of Pd leaching from the catalyst, in accordance with the ICP-AES results (Table S1, entry 5).

The reduction route and the intermediate species that evolved during the reaction over ZIF-8_C@Pd@ZIF-8 were investigated by DRIFTS. Upon introducing substrates with Ar flowing over the catalyst under reaction conditions, the DRIFT bands of the adsorbed nitrobenzene (~1563 and 1360 cm^{-1}) and hydrazine (~3100 cm^{-1}) continue to increase within 60 min. The bands at ~1507 and 1364 cm^{-1} attributed to σ_{N-O} and σ_{N-O-H} prove the formation of Ph-NO and Ph-NOH intermediates (Figure 3a).[19] After purging for approximately 10 min, a new peak at ~3300 cm^{-1} appeared, which was assigned to σ_{N-H} belonging to the targeted product. The results prove that the hydrogenation of nitroaromatic compounds to arylamine undergoes a phenylhydroxylamine pathway, indicating the possible reaction pathway of *p*-CNB hydrogenation (Figure S20).

To further illustrate how the different Pd electronic states created by the interfacial facet engineering of ZIF-8 dominate the selectivity, the DRIFTS of competitive adsorption for chlorobenzene and nitrobenzene on ZIF-8_C@Pd@ZIF-8 and ZIF-8_{RD}@Pd@ZIF-8 have been performed (Figure 3b and c). In the beginning, the DRIFTS for ZIF-8_C@Pd@ZIF-8 includes a band at 737 cm^{-1} ascribed to the C–Cl bond of chlorobenzene and the characteristic bands at 1529 and 1347 cm^{-1} assignable to the N=O bond of nitrobenzene. Upon purging with Ar gas, the signal of nitrobenzene is maintained while the peak associated with C–Cl gradually disappears, suggesting the stronger adsorption of N=O compared to that of C–Cl over ZIF-8_C@Pd@ZIF-8 (Figure 3b). For ZIF-8_{RD}@Pd@ZIF-8, DRIFTS reveals bands associated with both the N=O and C–Cl bonds, indicating simultaneous physical adsorption of nitrobenzene and chlorobenzene, which is similar to ZIF-8_C@Pd@ZIF-8. However, signals associated with nitrobenzene and chlorobenzene are maintained (~1529, 1347, and 737 cm^{-1}) even after purging with Ar gas for 60 min, indicating that both substrates are strongly adsorbed over ZIF-8_{RD}@Pd@ZIF-8 (Figure 3c), in which the peak at ~737 cm^{-1} related to the C–Cl bond is much stronger than the other two peaks associated with the N=O bond, and distinctly different from what is observed for ZIF-8_C@Pd@ZIF-8 (Figure 3b). Given the negative charge of $-NO_2$ (−0.238 e) in nitrobenzene and –Cl (−0.104 e) in chlorobenzene according to the previous report,[9e] following Coulomb's law, $-NO_2$ rather than the C–Cl group would be more preferably adsorbed on the more electron-deficient Pd in ZIF-8_C@Pd@ZIF-8; by contrast, both $-NO_2$ and C–Cl groups can be simultaneously adsorbed on Pd in ZIF-8_{RD}@Pd@ZIF-8, accordingly leading to a discrepancy in catalytic selectivity.

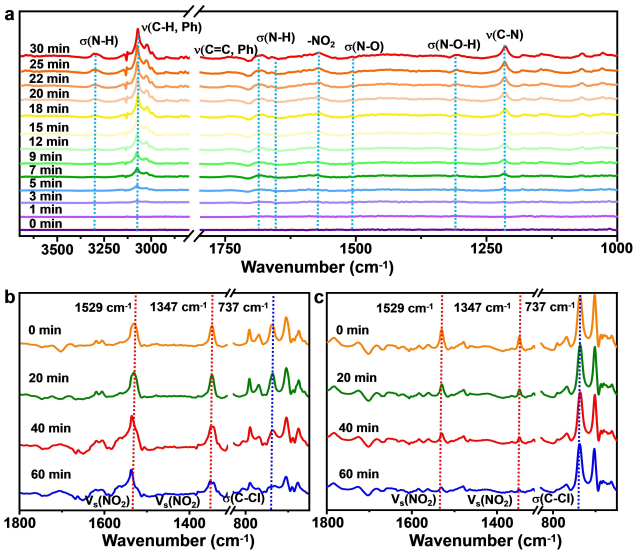

Figure 3. a) The in situ DRIFTS of 3700–1000 cm^{-1} for detecting the reaction intermediates in the nitrobenzene reduction over ZIF-8_C@Pd@ZIF-8 in the presence of hydrazine vapor purged by Ar gas at 85 °C for 30 min. DRIFTS of competitive adsorption for mixed nitrobenzene and chlorobenzene over b) ZIF-8_C@Pd@ZIF-8 and c) ZIF-8_{RD}@Pd@ZIF-8, respectively.

Encouraged by the outstanding catalytic performance of ZIF-8_C@Pd@ZIF-8 in the hydrogenation of *p*-CNB, similar substrates with other halogen groups at different positions have also been investigated (Figure S21). Substrates *o*-chloronitrobenzene, *m*-chloronitrobenzene, and 2,4-dichloronitrobenzene were completely converted into the corresponding haloanilines with ~97 % selectivity, where 2,4-dichloronitrobenzene has been demonstrated to be able to pass through the ZIF-8 shell (Figure S22). Upon replacement of –Cl with –F or –Br, *p*-fluoronitrobenzene and *p*-bromonitrobenzene can also be transformed into the corresponding haloanilines with ~96 % selectivity. These results indicate that excellent conversion for all the substituted substrates and very high selectivity to the corresponding haloanilines can be achieved, demonstrating excellent chemoselectivity in the reduction of the nitro group in the presence of reducible functional halogen groups. These data support the general applicability and tolerance for a variety of substituents (*meta*-, *ortho*-, and *para*-) of the substrates in the selective hydrogenation over ZIF-8_C@Pd@ZIF-8, which is explained by the specific and selective adsorption of the nitro group in the corresponding halonitrobenzenes on the Pd sites in ZIF-8_C@Pd@ZIF-8, as clearly illustrated above. In addition, other substrates, such as 4-nitrobenzonitrile and 4-nitroanisole, can also be converted to the corresponding anilines with ~97 % selectivity, demonstrating the superiority of ZIF-8_C@Pd@ZIF-8 (Figure S21). These results reveal that the chemical microenvironment around Pd NPs, regulated by ZIF-8 facet engineering, can improve catalytic activity and optimize the selectivity by preferential adsorption of the $-NO_2$ group.

Conclusion

In summary, a series of ZIF-8_X@Pd@ZIF-8 composites with a ZIF-8 core bearing engineered crystal facets have been successfully constructed for hydrogenation of halonitrobenzenes. Due to enhanced interfacial electron transfer, the Pd NPs in ZIF-8_C@Pd@ZIF-8 are more positively charged than those in ZIF-8_{TRD}@Pd@ZIF-8 and ZIF-8_{RD}@Pd@ZIF-8, accounting for superior hydrogenation activity and high selectivity to the corresponding haloanilines. Remarkably,

the electronic state of supported Pd NPs is dominated by the exposed facet of ZIF-8, in which the positively charged Pd sites are favorable to the preferential $-NO_2$ group adsorption of substituted nitroarenes, leading to high selectivity to the target products. This work opens an avenue to the electronic state regulation of supported metal catalysts by facet engineering of the supports toward optimized performance in heterogeneous catalysis.

Acknowledgements

This work was supported by the National Key Research and Development Program of China (2021YFA1500402), the National Natural Science Foundation of China (21725101, 21871244, 22161142001, and 22101269), International Partnership Program of CAS (211134KYSB20190109), and Collaborative Innovation Program of Hefei Science Center, CAS (2020HSC-CIP005).

Conflict of Interest

The authors declare no conflict of interest.

Data Availability Statement

The data that support the findings of this study are available from the corresponding author upon reasonable request.

Keywords: Crystal Facet Engineering · Electron Density · Metal Nanoparticles · Metal–Organic Frameworks · Microenvironment Modulation

[1] a) J. Zhang, L. Wang, Y. Shao, Y. Wang, B. C. Gates, F.-S. Xiao, *Angew. Chem. Int. Ed.* **2017**, *56*, 9747–9751; *Angew. Chem.* **2017**, *129*, 9879–9883; b) R. V. Jagadeesh, A.-E. Surkus, H. Junge, M.-M. Pohl, J. Radnik, J. Rabeah, H. Huan, V. Schünemann, A. Brückner, M. Beller, *Science* **2013**, *342*, 1073–1076; c) C. Wang, S. Mao, Z. Wang, Y. Chen, W. Yuan, Y. Ou, H. Zhang, Y. Gong, Y. Wang, B. Mei, Z. Jiang, Y. Wang, *Chem* **2020**, *6*, 752–765.

[2] a) F. Cárdenas-Lizana, Y. Hao, M. Crespo-Quesada, I. Yuranov, X. Wang, M. A. Keane, L. Kiwi-Minsker, *ACS Catal.* **2013**, *3*, 1386–1396; b) H. Wei, X. Liu, A. Wang, L. Zhang, B. Qiao, X. Yang, Y. Huang, S. Miao, J. Liu, T. Zhang, *Nat. Commun.* **2014**, *5*, 5634; c) W. Shi, B. Zhang, Y. Lin, Q. Wang, Q. Zhang, D. S. Su, *ACS Catal.* **2016**, *6*, 7844–7854; d) M. Pietrowski, M. Wojciechowska, *Catal. Today* **2009**, *142*, 211–214; e) F. Cárdenas-Lizana, X. Wang, D. Lamey, M. Li, M. A. Keane, L. Kiwi-Minsker, *Chem. Eng. J.* **2014**, *255*, 695–704; f) M. Boronat, P. Concepción, A. Corma, S. González, F. Illas, P. Serna, *J. Am. Chem. Soc.* **2007**, *129*, 16230–16237.

[3] a) K. Liu, R. Qin, N. Zheng, *J. Am. Chem. Soc.* **2021**, *143*, 4483–4499; b) T. W. van Deelen, C. Hernández Mejía, K. P. de Jong, *Nat. Catal.* **2019**, *2*, 955–970; c) M. Tang, S. Li, S. Chen, Y. Ou, M. Hiroaki, W. Yuan, B. Zhu, H. Yang, Y. Gao, Z. Zhang, Y. Wang, *Angew. Chem. Int. Ed.* **2021**, *60*, 22339–22344; *Angew. Chem.* **2021**, *133*, 22513–22518; d) G. Li, S. Zhao, Y. Zhang, Z. Tang, *Adv. Mater.* **2018**, *30*, 1800702.

[4] a) J. Zhang, M. Wang, Z. Gao, X. Qin, Y. Xu, Z. Wang, W. Zhou, D. Ma, *J. Am. Chem. Soc.* **2022**, *144*, 5108–5115; b) L. Liu, A. Corma, *Chem. Rev.* **2018**, *118*, 4981–5079; c) Z. Li, S. Ji, Y. Liu, X. Cao, S. Tian, Y. Chen, Z. Niu, Y. Li, *Chem. Rev.* **2020**, *120*, 623–682; d) S. Mitchell, J. Pérez-Ramírez, *Nat. Rev. Mater.* **2021**, *6*, 969–985; e) Y. Wang, C. Wang, L. Wang, L. Wang, F.-S. Xiao, *Acc. Chem. Res.* **2021**, *54*, 2579–2590; f) Y. Pan, Y. Qian, X. Zheng, S.-Q. Chu, Y. Yang, C. Ding, X. Wang, S.-H. Yu, H.-L. Jiang, *Natl. Sci. Rev.* **2021**, *8*, nwaa224.

[5] a) X. Huang, C. Dang, H. Yu, H. Wang, F. Peng, *ACS Catal.* **2015**, *5*, 1155–1163; b) L. Jiang, K. Liu, S. F. Hung, L. Zhou, R. Qin, Q. Zhang, P. Liu, L. Gu, H. M. Chen, G. Fu, N. Zheng, *Nat. Nanotechnol.* **2020**, *15*, 848–853.

[6] a) Y. Zhang, J. Zhang, B. Zhang, R. Si, B. Han, F. Hong, Y. Niu, L. Sun, L. Li, B. Qiao, K. Sun, J. Huang, M. Haruta, *Nat. Commun.* **2020**, *11*, 558; b) M. Cargnello, V. V. T. Doan-Nguyen, T. R. Gordon, R. E. Diaz, E. A. Stach, R. J. Gorte, P. Fornasiero, C. B. Murray, *Science* **2013**, *341*, 771–773; c) F. Jiang, S. Wang, B. Liu, J. Liu, L. Wang, Y. Xiao, Y. Xu, X. Liu, *ACS Catal.* **2020**, *10*, 11493–11509; d) Y. Zhang, J.-X. Liu, K. Qian, A. Jia, D. Li, L. Shi, J. Hu, J. Zhu, W. Huang, *Angew. Chem. Int. Ed.* **2021**, *60*, 12074–12081; *Angew. Chem.* **2021**, *133*, 12181–12188.

[7] a) M. Zhao, K. Yuan, Y. Wang, G. Li, J. Guo, L. Gu, W. Hu, H. Zhao, Z. Tang, *Nature* **2016**, *539*, 76–80; b) H. Liu, L. Chang, L. Chen, Y. Li, *ChemCatChem* **2016**, *8*, 946–951; c) Y. Yun, H. Sheng, K. Bao, L. Xu, Y. Zhang, D. Astruc, M. Zhu, *J. Am. Chem. Soc.* **2020**, *142*, 4126–4130.

[8] a) H. Furukawa, K. E. Cordova, M. O'Keeffe, O. M. Yaghi, *Science* **2013**, *341*, 1230444; b) H.-C. Zhou, S. Kitagawa, *Chem. Soc. Rev.* **2014**, *43*, 5415–5418; c) T. Islamoglu, S. Goswami, Z. Li, A. J. Howarth, O. K. Farha, J. T. Hupp, *Acc. Chem. Res.* **2017**, *50*, 805–813; d) H. Li, L. Li, R.-B. Lin, W. Zhou, Z. Zhang, S. Xiang, B. Chen, *EnergyChem* **2019**, *1*, 100006; e) L. Jiao, J. Wang, H.-L. Jiang, *Acc. Mater. Res.* **2021**, *2*, 327–339; f) Y. Chen, Y.-J. Chen, Y. Qi, H.-J. Zhu, X. Huang, Y.-R. Wang, R.-X. Yang, Y.-H. Kan, S.-L. Li, Y.-Q. Lan, *Chem* **2021**, *7*, 463–479; g) A. Dhakshinamoorthy, A. M. Asiri, H. García, *Trends Chem.* **2020**, *2*, 454–466.

[9] a) A. Aijaz, A. Karkamkar, Y. J. Choi, N. Tsumori, E. Rönnebro, T. Autrey, H. Shioyama, Q. Xu, *J. Am. Chem. Soc.* **2012**, *134*, 13926–13929; b) G. Lu, S. Li, Z. Guo, O. K. Farha, B. G. Hauser, X. Qi, Y. Wang, X. Wang, S. Han, X. Liu, J. S. DuChene, H. Zhang, Q. Zhang, X. Chen, J. Ma, S. Loo, W. D. Wei, Y. Yang, J. T. Hupp, F. Huo, *Nat. Chem.* **2012**, *4*, 310–316; c) X. Li, T. Goh, L. Li, C. Xiao, Z. Guo, X. Zeng, W. Huang, *ACS Catal.* **2016**, *6*, 3461–3468; d) Q. Yang, Q. Xu, H.-L. Jiang, *Chem. Soc. Rev.* **2017**, *46*, 4774–4808; e) L. Li, Z. Li, W. Yang, Y. Huang, G. Huang, Q. Guan, Y. Dong, J. Lu, S.-H. Yu, H.-L. Jiang, *Chem* **2021**, *7*, 686–698; f) F. Chen, K. Shen, J. Chen, X. Yang, J. Cui, Y. Li, *ACS Cent. Sci.* **2019**, *5*, 176–185.

[10] a) X.-C. Huang, Y.-Y. Lin, J.-P. Zhang, X.-M. Chen, *Angew. Chem. Int. Ed.* **2006**, *45*, 1557–1559; *Angew. Chem.* **2006**, *118*, 1587–1589; b) K. S. Park, Z. Ni, A. P. Côté, J. Y. Choi, R. Huang, F. J. UribeRomo, H. K. Chae, M. O'Keeffe, O. M. Yaghi, *Proc. Natl. Acad. Sci. USA* **2006**, *103*, 10186–10191.

[11] a) S. R. Venna, J. B. Jasinski, M. A. Carreon, *J. Am. Chem. Soc.* **2010**, *132*, 18030–18033; b) C. Avci, I. Imaz, A. Carné-Sánchez, J. A. Pariente, N. Tasios, J. Pérez-Carvajal, M. I. Alonso, A. Blanco, M. Dijkstra, C. López, D. Maspoch, *Nat. Chem.* **2018**, *10*, 78–84; c) X.-Y. Liu, W.-S. Lo, C. Wu, B. P. Williams, L. Luo, Y. Li, L.-Y. Chou, Y. Lee, C.-K. Tsung, *Nano Lett.* **2020**, *20*, 1774–1780.

[12] L. Li, W. Yang, Q. Yang, Q. Guan, J. Lu, S.-H. Yu, H.-L. Jiang, *ACS Catal.* **2020**, *10*, 7753–7726.

[13] K. Jang, S.-H. Kim, H. Jun, C. Jung, J. Yu, S. Lee, P.-P. Choi, *Nat. Commun.* **2021**, *12*, 4301.

[14] D. Chen, W. Yang, L. Jiao, L. Li, S.-H. Yu, H.-L. Jiang, *Adv. Mater.* **2020**, *32*, 2000041.
[15] a) F. Cárdenas-Lizana, Y. F. Hao, M. Crespo-Quesada, I. Yuranov, X. D. Wang, M. A. Keane, L. Kiwi-Minsker, *ACS Catal.* **2013**, *3*, 1386–1396; b) X. Zhang, Q. Gu, Y. Ma, Q. Guan, R. Jin, H. Wang, B. Yang, J. Lu, *J. Catal.* **2021**, *400*, 173–183.
[16] a) Q. Zhang, J. Bu, J. Wang, C. Sun, D. Zhao, G. Sheng, X. Xie, M. Sun, L. Yu, *ACS Catal.* **2020**, *10*, 10350–10363; b) W. Zhang, W. Shi, W. Ji, H. Wu, Z. Gu, P. Wang, X. Li, P. Qin, J. Zhang, Y. Fan, T. Wu, Y. Fu, W. Zhang, F. Huo, *ACS Catal.* **2020**, *10*, 5805–5813.
[17] a) S. K. Singh, X.-B. Zhang, Q. Xu, *J. Am. Chem. Soc.* **2009**, *131*, 9894–9895; b) J. Wang, Y. Zhang, J. Diao, J. Zhang, H. Y. Liu, D. S. Su, *Chin. J. Catal.* **2018**, *39*, 79–87.
[18] a) D. Zhu, L. Zhang, R. E. Ruther, J. Hamers, *Nat. Mater.* **2013**, *12*, 836–841; b) C. Lv, C. Yan, G. Chen, Y. Ding, J. Sun, Y. Zhou, G. Yu, *Angew. Chem. Int. Ed.* **2018**, *57*, 6073–6076; *Angew. Chem.* **2018**, *130*, 6181–6184.
[19] a) F. Tian, Y. Cui, A. V. Teplyakov, *J. Phys. Chem. C* **2014**, *118*, 502–512; b) W. Liu, H. Feng, Y. Yang, Y. Niu, L. Wang, P. Yin, S. Hong, B. Zhang, X. Zhang, M. Wei, *Nat. Commun.* **2022**, *13*, 3188.

Manuscript received: July 30, 2022
Accepted manuscript online: September 27, 2022
Version of record online: October 19, 2022